

Characteristics of electronbeamexcited Xe* 2 at low pressures as a vacuum ultraviolet source

D. J. Eckstrom, H. H. Nakano, D. C. Lorents, T. Rothem, J. A. Betts, M. E. Lainhart, D. A. Dakin, and J. E. Maenchen

Citation: [Journal of Applied Physics](#) **64**, 1679 (1988); doi: 10.1063/1.342474

View online: <http://dx.doi.org/10.1063/1.342474>

View Table of Contents: <http://scitation.aip.org/content/aip/journal/jap/64/4?ver=pdfcov>

Published by the [AIP Publishing](#)

Articles you may be interested in

[Measurement and control of absolute nitrogen atom density in an electron-beam-excited plasma using vacuum ultraviolet absorption spectroscopy](#)

J. Appl. Phys. **88**, 1756 (2000); 10.1063/1.1305559

[Theoretical evaluation of a shortpulse electronbeamexcited XeF\(B→X\) laser using a lowpressure, room temperature Ar/Xe/F2 gas mixture](#)

J. Appl. Phys. **67**, 3932 (1990); 10.1063/1.345001

[Characteristics of electronbeamexcited Kr* 2 at low pressures as a vacuum ultraviolet source](#)

J. Appl. Phys. **64**, 1691 (1988); 10.1063/1.341762

[Lowenergy electron distribution in electronbeamexcited XeCl laser mixtures](#)

J. Appl. Phys. **64**, 500 (1988); 10.1063/1.341988

[Theoretical evaluation of electronbeamexcited vacuumultraviolet F2 lasers](#)

J. Appl. Phys. **59**, 1815 (1986); 10.1063/1.336405



Characteristics of electron-beam-excited Xe_2^* at low pressures as a vacuum ultraviolet source

D. J. Eckstrom, H. H. Nakano,^{a)} D. C. Lorents, and T. Rothem^{b)}
SRI International, Menlo Park, California 94025

J. A. Betts and M. E. Lainhart
TRW, Incorporated, Redondo Beach, California 90278

D. A. Dakin and J. E. Maenchen^{c)}
Physics International, San Leandro, California 94577

(Received 6 January 1988; accepted for publication 3 May 1988)

The performance of Xe_2^* as a 172-nm fluorescence or laser source when pumped by a low-current, long-pulse electron beam was determined. The fluorescence efficiency of Xe_2^* is near the theoretical limit of $\sim 50\%$ at modest pressures over a range of pump rates up to 10^6 W/cm. The laser efficiency is limited to values $< 1\%$ by a very strong medium absorption that is probably due to Xe_2^* photoionization. Laser performance is further degraded by early pulse termination that appears related to mirror degradation. An improved kinetics and extraction code was developed to model the performance of the Xe_2^* system. A key component of the model is a more detailed treatment of the interactions between secondary electrons and excited atomic and molecular xenon states. Rates for these processes were derived as described herein. With this model, good absolute agreement was obtained between experiments and calculated parameters at pressures as low as 0.5 atm.

I. INTRODUCTION

The concept of producing short-pulse, high-energy lasers suitable for generating inertial-confinement fusion through vacuum-ultraviolet (VUV) photodissociation of molecules to produce group-VI atomic lasers was first proposed by Murray and Rhodes,¹ who also identified the overlap between Ar_2^* radiation at 126 nm and the absorption of N_2O to produce $\text{O}(^1S)$, the overlap between Kr_2^* radiation at 146 nm and OCS absorption to produce $\text{S}(^1S)$, and the overlap between Xe_2^* radiation at 172 nm and OCSe absorption to produce $\text{Se}(^1S)$. Photolytic pumping of N_2O by Ar_2^* was subsequently used by Hughes, Olson, and Hunter² to demonstrate gain on the $\text{ArO}(^1S-^1D)$ transition. Basov and co-workers^{3,4} used VUV radiation from exploding wire discharges to achieve lasing on $\text{XeO}(^1S-^1D)$. Later Powell and co-workers used Xe_2^* pumping to achieve lasing on the $\text{Se}(^1S-^1D)$ and $\text{Se}(^1S-^3P)$ transitions⁵ and Kr_2^* pumping to produce lasing on $\text{S}(^1S-^1D)$ transition.⁶ In addition to these group-VI laser studies, Xe_2^* pumping was used to produce lasing on $\text{HgCl}(B-X)$,⁷ $\text{XeF}(B-X)$ ⁸ and $\text{XeF}(C-A)$ ^{9,10} transitions.

The Xe_2^* laser was the first excimer laser to be demonstrated.¹¹ In spite of its long history, however, many details of the kinetics and absorption properties of electron-beam-pumped xenon were unknown. Furthermore, with the exception of a study by Turner,¹² previous works utilized very high-current, short-pulse electron-beam pumping. The ob-

jective of the work described here was to assess the efficiency and scalability of "softly pumped" xenon as either a coherent (laser) or incoherent (fluorescence) VUV photolytic driver at 172 nm. This was accomplished by formulating a coupled kinetics and extraction code, and by carrying out a set of experiments that allowed verification of the accuracy of the code. This code was then used to calculate the potential efficiency of optimized photolytic drivers. Similar studies were reported in Refs. 13 and 14.

II. KINETIC MODEL

The first kinetic model for rare-gas excimer lasers was formulated by Lorents.¹⁵ Detailed application of this model with several improvements was made by Werner *et al.*^{16,17} The model used in this study is very similar to that described in Ref. 17, so we will give only a brief outline here except where differences occur. In particular, we have used some rates different from those of Werner *et al.*, but the major difference is that we have added a number of electron-excited state interactions and have estimated the rates for those processes. These reactions are particularly important in applying the model to the gas pressures and pumping rates of interest in this study. The Werner model was found to match experiments well only for pressures $p \geq 4$ atm,¹⁷ while our work was confined to $p < 3$ atm.

A. Production processes

As in previous studies, our estimates of the conversion of electron beam energy to excitation in xenon are based on the calculations of Peterson and Allen¹⁸ for similar processes in argon. We find that the fractional conversions of electron energy to ionization (Xe^+), Xe^* production [$\text{Xe}(6s^3P)$], and Xe^{**} production [$\text{Xe}(6p)$ and higher lying states] are

^{a)} Present address: Hewlett-Packard Corporate Division, 1501 Page Mill Road, Palo Alto, CA 94304.

^{b)} Permanent address: Israel Atomic Energy Commission, Soreq Nuclear Research Center, Yavne 70400, Israel.

^{c)} Present address: Sandia National Laboratories, Albuquerque, NM 87185.

0.55, 0.060, and 0.086, respectively, with the remainder of the energy residing in subexcitation secondary electrons. Since the energies of these states are 12.1, 9.4, and ~ 10.5 eV, respectively, the productions of Xe^+ , Xe^* , and Xe^{**} are 2.7×10^{17} , 3.8×10^{16} , and 4.9×10^{16} per joule of electron-beam energy deposited. The average energy per excited state for Xe is then 16.7 eV, the average subexcitation secondary electron energy is 6.6 eV, and the potential fluorescence efficiency of Xe_2^* (assuming that each excited state leads to an Xe_2^* photon at 7.2 eV) is 43%. Slightly different assumptions about the production of excited states lead to theoretical fluorescence efficiencies as high as 54%.¹⁵

B. Kinetic processes

A complete list of the kinetic processes considered in our model is given in Table I, together with the rates obtained from the literature, from our estimates, or deduced

from a comparison of the model with our experimental results (see Sec. V). These processes are shown schematically in Fig. 1 and can be described briefly as follows.

The cascade of excitation from Xe^+ , Xe^{**} , and Xe^* to Xe_2^* is described by reactions 1–9. Reactions 10 and 11 describe the mixing of singlet and triplet excimers, Xe_2^* ($^1\Sigma$) and Xe_2^* ($^3\Sigma$), by electrons and neutrals, respectively. Reactions 12–15 indicate spontaneous emission and photoionization of the Xe_2^* excimers (stimulated emission is discussed below). These reactions have all been included in previous models, and are described in detail in Refs. 15 and 17. Literature values for the rate constants were used when available. Reactions 16–17 and 30–31 are Penning ionization loss processes, while reactions 25 and 29 represent radiative cascade and photoionization of the second excited state Xe^{**} . Photoionization of Xe_2^* (reaction 34) was also considered in some cases.

Reactions 18–24, 26–28, and 32–33 are new additions to

TABLE I. Kinetic model for xenon.

Reaction	Rate ^a	Reference	Sensitivity
1. $\text{Xe}^+ + 2\text{Xe} \rightarrow \text{Xe}_2^+ + \text{Xe}$	$2 \times 10^{-34} (300/T_g)^{1/2}$	19,20	
2. $\text{Xe}_2^+ + 2\text{Xe} \rightarrow \text{Xe}_3^+ + \text{Xe}$	$6 \times 10^{-32} (300/T_g)^{1/2}$	21	
3. $\text{Xe}_2^+ + e \rightarrow \text{Xe}^{**} + \text{Xe}$	$2.3 \times 10^{-7} T_e^{-0.7}$	22	
4. $\text{Xe}_3^+ + e \rightarrow \text{Xe}^{**} + 2\text{Xe}$	$1 \times 10^{-5} T_e^{-0.5}$	21	
5. $\text{Xe}^{**} + 2\text{Xe} \rightarrow \text{Xe}_2^{**} + \text{Xe}$	$5 \times 10^{-31} (300/T_g)^{1/2}$	Best fit	Affects fit strongly
6. $\text{Xe}_2^{**} \rightarrow \text{Xe}^* + \text{Xe}$	1×10^8	Best fit	Moderate effect on risetime
7. $\text{Xe}_2^{**} + \text{Xe} \rightarrow \text{Xe}^* + 2\text{Xe}$	$1 \times 10^{-11} (T_g/300)^{1/2}$	Best fit	
8. $\text{Xe}^* + 2\text{Xe} \rightarrow \text{Xe}_2^{(3)} + \text{Xe}$	$4.4 \times 10^{-32} (300/T_g)^{1/2}$ ^b	23,24	Strong effect on rise and decay
9. $\text{Xe}^* + 2\text{Xe} \rightarrow \text{Xe}_2^{(1)} + \text{Xe}$	$2 \times 10^{-32} (300/T_g)^{1/2}$ ^b	25	
10a. $e + \text{Xe}_2^{(3)} \rightarrow e + \text{Xe}_2^{(1)}$	1.8×10^{-8} ^c	Appendix ($\times 0.1$)	Regulates decay
10b. $e + \text{Xe}_2^{(1)} \rightarrow e + \text{Xe}_2^{(3)}$	4.9×10^{-8} ^c	Appendix ($\times 0.1$)	
11a. $\text{Xe}_2^{(1)} + \text{Xe} \rightarrow \text{Xe}_2^{(3)} + \text{Xe}$	$4.6 \times 10^{-15} (T_g/300)^{1/2}$	25	
11b. $\text{Xe}_2^{(3)} + \text{Xe} \rightarrow \text{Xe}_2^{(1)} + \text{Xe}$	$1.2 \times 10^{-13} (T_g/300)^{1/2}$	25	
12. $\text{Xe}_2^{(1)} \rightarrow 2\text{Xe} + h\nu$	2.1×10^8	25	
13. $\text{Xe}_2^{(3)} \rightarrow 2\text{Xe} + h\nu$	1×10^7	25	
14. $\text{Xe}_2^{(1)} + h\nu \rightarrow \text{Xe}_2^+ + e$	$2 \times 10^{-18} \text{ cm}^2$	26,27	Reduces gain
15. $\text{Xe}_2^{(3)} + h\nu \rightarrow \text{Xe}_2^+ + e$	$2 \times 10^{-18} \text{ cm}^2$	26,27	May be $3.5 \times 10^{-18} \text{ cm}^2$
16. $2\text{Xe}_2^* \rightarrow \text{Xe}_2^+ + 2\text{Xe} + e$	8×10^{-11}	28	
17. $2\text{Xe}^* \rightarrow \text{Xe}^+ + \text{Xe} + e$	8×10^{-11}	28	
18. $\text{Xe}_2^* + e \rightarrow \text{Xe}_2^+ + 2e$	5×10^{-9} ^c	Appendix	Insensitive
19. $\text{Xe}^* + e \rightarrow \text{Xe}^+ + 2e$	2.7×10^{-9} ^c	Appendix	Insensitive
20. $\text{Xe}_2^* + e \rightarrow 2\text{Xe} + e$	4×10^{-9} ^c	Appendix ($\times 3$)	
21. $\text{Xe}^* + e \rightarrow \text{Xe} + e$	3×10^{-9} ^c	Appendix ($\times 3$)	Very sensitive, principal loss
22. $\text{Xe}_2^* + e \rightarrow \text{Xe}^* + \text{Xe} + e$	2×10^{-7} ^c	Appendix	Shifts peak fluorescence time
23. $\text{Xe}_2^* + e \rightarrow \text{Xe}_2^{**} + e$	3×10^{-7} ^c	Appendix	
24a. $\text{Xe}_2^{**} + e \rightarrow \text{Xe}_2^{(3)} + e$	6×10^{-7} ^c	Appendix	
24b. $\text{Xe}_2^{**} + e \rightarrow \text{Xe}_2^{(1)} + e$	2×10^{-7} ^c	Appendix	
25. $\text{Xe}^{**} \rightarrow \text{Xe}^* + h\nu$	$< 1 \times 10^6$	Estimate	
26. $\text{Xe}^{**} + e \rightarrow \text{Xe}^+ + 2e$	2×10^{-8} ^c	Appendix	
27. $\text{Xe}^* + e \rightarrow \text{Xe}^{**} + e$	3×10^{-7} ^c	Appendix	
28. $\text{Xe}^{**} + e \rightarrow \text{Xe}^* + e$	8×10^{-7} ^c	Appendix	
29. $\text{Xe}^{**} + h\nu \rightarrow \text{Xe}^+ + e$	$1 \times 10^{-18} \text{ cm}^2$	26	
30. $2\text{Xe}^{**} \rightarrow \text{Xe}^+ + \text{Xe} + e$	1×10^{-10}	28	
31. $2\text{Xe}_2^{**} \rightarrow \text{Xe}_2^+ + 2\text{Xe} + e$	1×10^{-10}	28	
32. $\text{Xe}_2^+ + e \rightarrow \text{Xe}^+ + \text{Xe} + e$	1×10^{-7} ^c	Appendix	
33. $\text{Xe}_2^{**} + e \rightarrow \text{Xe}_2^+ + 2e$	6×10^{-8} ^c	Appendix	
34. $\text{Xe}_2^{**} + h\nu \rightarrow \text{Xe}_2^+ + e$	$1 \times 10^{-18} \text{ cm}^2$	26	

^a Units are cm^6/s , cm^3/s , s^{-1} , or cm^2 (where noted) as appropriate.

^b Xe^* includes the $6s^3P_2$ and $6s^3P_1$ states, which are assumed to be in statistical equilibrium. The $6s^3P_0$ and $6s^1P_1$ levels are lumped with Xe^{**} .

^c At $T_e = 1$ eV.

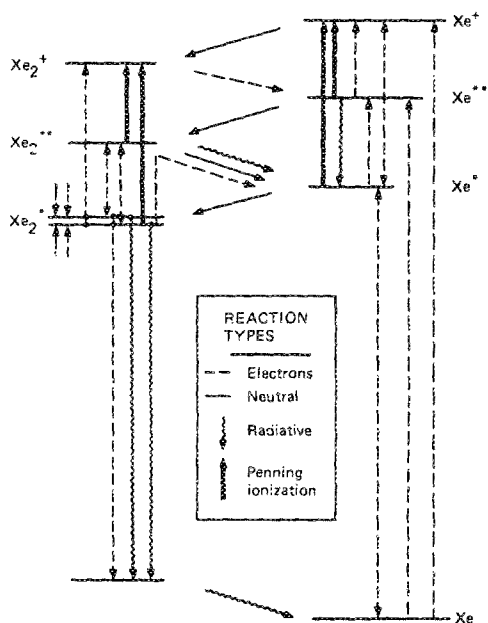


FIG. 1. Schematic representation of the kinetic model for *e*-beam-pumped xenon.

the kinetic model, representing interactions of secondary electrons with excited atomic and molecular states to cause state mixing, ionization, dissociation, and superelastic quenching. We estimated the electron-energy-dependent cross sections for these reactions, as well as for the singlet-triplet excimer mixing process (reaction 10), as described in the Appendix, and then calculated rates by integrating the cross sections over a Maxwellian electron velocity distribution. The rates so derived are presented in the Appendix; the values shown in Table I are for $T_e = 1$ eV. These processes were found to be very important in achieving agreement between kinetic model calculations and experiments.

C. Energy balance

Many of the neutral species reactions and all of the electron reactions have rates that are functions of T_g or T_e , respectively, as indicated in Table I. Accordingly, the kinetics code calculated T_g and T_e as a function of time and used kinetic rates appropriate to the instantaneous temperature. The neutral gas temperature rise is due to the net exothermicity of the reactions in Table I, and can be calculated in a straightforward manner. Calculated temperature rises were always < 200 K and usually < 100 K for the conditions of our experiments.

The energy balance equation for electrons considers energy transfer to and from the electron bath, as well as production and loss of electrons with finite energies. Electron energy source terms include secondary electron production with average energies of 6.6 eV, Penning ionization and photoionization of excited atomic and molecular states, and superelastic quenching collisions of electrons with excimers and excited states. Electron energy loss terms include excitation and ionization of excimers and excited states and elastic

collisions with the background gas. We do not include production of excited states from ground-state Xe by the high-energy tail of the secondary electron distribution or by electrons heated by superelastic collisions.

The electron-neutral elastic cooling rate is based on momentum transfer cross sections for *e*-Xe collisions. We assume that the electron energy distribution is Maxwellian, and have convolved the energy-dependent cross sections with such an energy distribution to calculate rates for elastic energy exchange between electrons and neutrals.

The use of a Maxwellian electron distribution for calculating rate constants from energy-dependent cross sections was justified by Boltzmann calculations performed using the code developed by Morgan,²⁹ and by comparison with calculations of Elliot and Green.³⁰ In these calculations, the time evolution of electron energy distributions in electron-beam-generated Xe and Ar plasmas was determined. Electron-neutral elastic and inelastic collisions, electron-electron collisions, and electron-ion dissociative recombination were included. These calculations showed that a Maxwellian model is a good approximation except at very short times and at times after the removal of the electron beam. Since, in the studies conducted in this program, steady state electron beam conditions applied for $\sim 1 \mu s$, the Maxwellian model should be a reasonable approximation.

D. Extraction

Our treatment of laser energy extraction was essentially the same as that described by Werner *et al.*¹⁷ Morse potentials were assumed for the singlet and triplet excimer states, a repulsive potential was used for the lower level, and wave functions were calculated using the expressions of Heaps and Herzberg.³¹ The stimulated emission cross section for a single vibrational-rotational upper state was calculated using the expression derived by Mies.³² Contributions from the various levels were summed to determine the cross section as a function of frequency. These frequency-dependent cross sections were used to calculate gain, laser intensity, and excited-state population depletion as a function of time, taking into account absorptions in the laser medium due to photoionization of excited states (reactions 14, 15, 29, and 34), an arbitrary nonsaturable absorption α (cm^{-1}), and losses due to outcoupling through and absorption by the cavity mirrors. These calculations were carried out at equally spaced frequency intervals, and the results were integrated numerically to give the total lasing intensity and excited-state population depletion due to stimulated emission.

III. EXPERIMENTS

A. Apparatus

The electron-beam source for these experiments was a Physics International Pulserad Model 420MR Marx run-down device capable of providing beam currents up to 20 A/ cm^2 with pulse lengths in excess of $1 \mu s$. The cathode emitter length was 107 cm, and the beam was apertured in this work to 100 cm length \times 2 cm height. One-mil Ti foils were supported on a stainless-steel hibachi structure which had 90% geometric transparency. Microdensitometer traces of x-ra-

diographic photographs show that the beam current was uniform over its length to $\pm 20\%$. In these experiments, the anode-cathode gap was varied from 10 to 5.2 cm to produce current densities from 5 to 18 A/cm².

A schematic diagram of the experimental apparatus is shown in Fig. 2. The test cell was constructed from stainless steel; the gas cell cavity was 2.5 cm high \times 3.2 cm deep \times 100 cm long. It was fitted with a shielded stripline Rogowski probe which allowed a measurement of the time history of the total current entering the cell on each shot. This history was used, together with the energy deposition measurements described below, to determine the *e*-beam pump rate history for each shot. The Rogowski probe was calibrated to measure absolute *e*-beam current (averaged over the length of the cell). However, the absolute calibration was valid only when firing into a vacuum; when the test cell was filled with gas, return currents reduced the measured Rogowski signal, with the fractional reduction increasing with gas pressure. In spite of this effect, we assume that the time history of the Rogowski signal accurately represents the time history of the *e*-beam current averaged over the length of the cell.

The test gas consisted either of pure xenon or of xenon-argon mixtures. The xenon was research grade (99.995%), while the argon was ultrahigh pure (99.999%). The gas passed through a pair of traps prior to entering the cell; the first trap was filled with molecular sieve material No. 7 and was held at dry ice temperature, while the second trap was filled with copper wool at 300 °C. When gas mixtures were used, they were formed by flowing each gas through a calibrated flowmeter and then merging them in a common fill line in order to ensure uniform mixing. The cell was evacuated to less than 2×10^{-5} Torr prior to filling. All the data reported here are based on the first shot into a gas fill, since there was a 20%–30% falloff of sidelight fluorescence on the second and subsequent shots.

B. Fluorescence intensity measurements

The optical axis was 2.0 cm from the foil. Absolute sidelight fluorescence intensities (photons/cm³ s) were mea-

sured using an ITT F4115 solar blind photodiode mounted perpendicular to the cell axis as shown in Fig. 2. The emitting volume and the solid angle were defined with apertures of 0.32 and 0.64 cm diameter, respectively. The quantum efficiencies of the photodiodes used were calibrated as a function of wavelength and applied voltage by comparison with an NBS standard.³³

The local energy deposition rate in the gas can be determined by adding the contributions which appear as radiation and as heat, with the latter component manifested as a pressure rise. The energy radiated per unit volume at the observation point in the cell was measured as the time integral of the absolute fluorescence histories described above. In a constant volume region, the pressure rise is related to the energy deposited as heat as $\Delta p(\text{atm}) = (20/3)\Delta H(\text{J/cm}^3)$. The pressure rise in each experiment was measured using a Validyne DP-15 transducer, for which the sensitivity and time response to transient pressure pulses were verified using acoustic waves generated in a shock tube. We assumed that the pressure rises measured were related to the energy deposited as heat averaged over the cross section of the cell. We then defined a factor β which was the ratio of the energy deposited locally in the optical observation region to the average energy deposition throughout the cell. This β factor was determined analytically using SANDYL code calculations³⁴ for our cell geometry and experimental conditions.

All the data reported here were analyzed based on the Validyne pressure-rise measurement and the SANDYL-calculated β factor. More recent measurements, reported separately,³⁵ show that the Validyne measurement does not accurately represent the average pressure rise in the cell when the pressure gradient across the cell is sharp (i.e., when the range of electrons is smaller than the cell depth), as is the case for even modest xenon pressures. Furthermore, β factors calculated by the SANDYL code seem to be in disagreement with the experimentally determined pressure distribution. Fortunately, the errors were partially self-cancelling; even so, this introduces some uncertainty into fluorescence yields reported below, particularly at the higher xenon pressure.

C. Laser studies

Laser performance tests were conducted using internal mirrors spaced 180 cm apart at the ends of extension tubes on the cell. The optical axis was again 2 cm from the *e*-beam foil. The mirrors, of 25 mm diameter and 2 m concave radius of curvature, were made by ACTON, and were dielectric coated for maximum reflection at 172 nm. Reflectivities of $R \geq 96\%$, and transmission $T \sim 2\%$ were achieved. Both MgF₂ and fused silica substrates were used. The optical cavity was aligned for each shot using a HeNe laser after filling the cell to the desired pressure. Laser spectra were recorded by splitting a fraction of the beam into a McPherson 218 $\frac{1}{4}$ -m monochromator fitted with a PAR optical multichannel analyzer (SIT), which in turn was fitted with a UV scintillator. Laser intensity histories were recorded using a second calibrated VUV photodiode (ITT F4115). A six-layer screen forming a neutral density filter of $T = 7 \times 10^{-4}$ was used to prevent saturation of the photodiode.

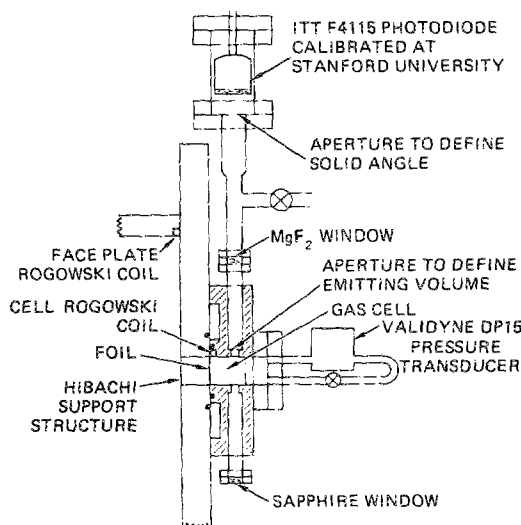


FIG. 2. Schematic cross section of experimental apparatus.

D. Electron density measurement

A set of measurements was carried out aimed at measuring electron densities by the inverse bremsstrahlung absorption technique.³⁶ In these tests, the VUV laser mirrors were replaced with NaCl windows, and the beam from a cw CO₂ laser operating at about 5 W was passed through the cell and transmitted into the screen room where it impinged on a HgCdTe detector (which is nominally sensitive from 6 to 14 μm). The absorption of the laser beam can be related to the xenon pressures, the electron density, and electron energy distribution.³⁶

E. Gain measurements

Experiments were also carried out in an attempt to measure gain and/or absorption as a function of time and wavelength in the test gas using the single-pass versus double-pass intensity measurement technique described by Gerardo and Johnson.^{37,38} In these tests, the cell was fitted with MgF₂ end windows, and a VUV monochromator was attached to each end of the cell. Apertures in the cell and at each end window defined the viewed volume and the solid angle. At one monochromator, an enhanced aluminum flat mirror of $R \approx 80\%$ with a 0.32-cm central hole (ACTON) served as the aperture and as the reflector for the double-pass intensity measurement. These measurements showed clear evidence of gain, but they were not reproducible enough to obtain quantitative results. The measurements are very sensitive to the spatial and temporal behavior of the *e*-beam current, and it seems that the nonuniformities in our *e*-beam source were sufficiently large to preclude useful results. Therefore, these measurements are not discussed further.

IV. RESULTS AND DISCUSSION

In this section, we describe the experimental results and the comparative results obtained from the kinetics code, and discuss insofar as possible the physical processes governing the observed behavior as deduced from the code calculations.

A. Fluorescence histories

Absolute sidelight fluorescence histories are presented in Figs. 3–5 for xenon pressures of $\frac{1}{2}$, 1, and 3 atm, respectively. Each figure presents results for two current densities (pump rates). Also included in the figures are the excited-state production (pump) rate histories and the fluorescence histories predicted by the kinetic code. The pump rates are presented as excited states produced per cm³ per second; these values are based on the energy deposition rate in W/cm³ measured from the total energy deposition for each shot, the *e*-beam current history for that shot, and the SANDYL β factor as described above. Again, the conversion from W/cm³ to excited states per cm³ per sec was based on the estimate of an average energy of 16.7 eV per excited state for *e*-beam-excited xenon. Presentation of both the pump rate and fluorescence rate histories allows ready comparison of kinetic response times and of fluorescence efficiencies of xenon. It should be emphasized that the current history used to calculate the pump rate was an average over the entire 100-cm

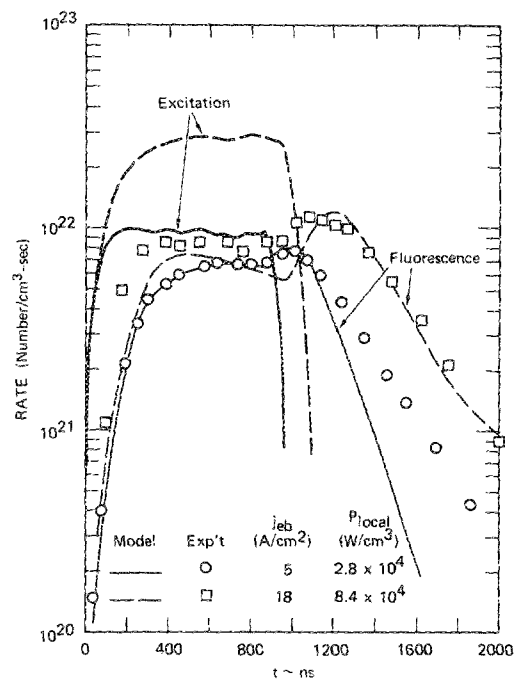


FIG. 3. Excitation rate and excimer fluorescence rate histories for *e*-beam-pumped xenon at 0.5 atm. Excitation rates apply to both the experiments and the model.

cell, while fluorescence was sampled from only a 0.3 cm portion, so fluctuations in one parameter may not appear in the other. We estimate that the uncertainties of the pump and fluorescence rates are $\pm 10\%$.

The general trend observed in Figs. 3–5 is that the fluorescence rate follows the pump rate more closely in both

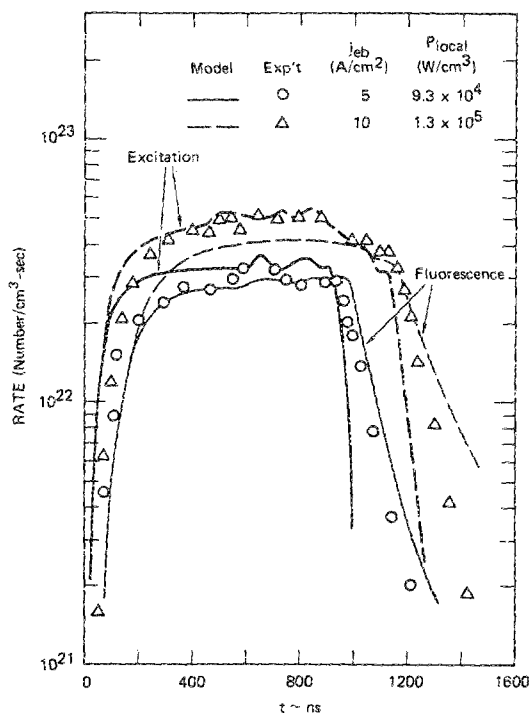


FIG. 4. Excitation rate and excimer fluorescence rate histories for *e*-beam-pumped xenon at 1 atm.

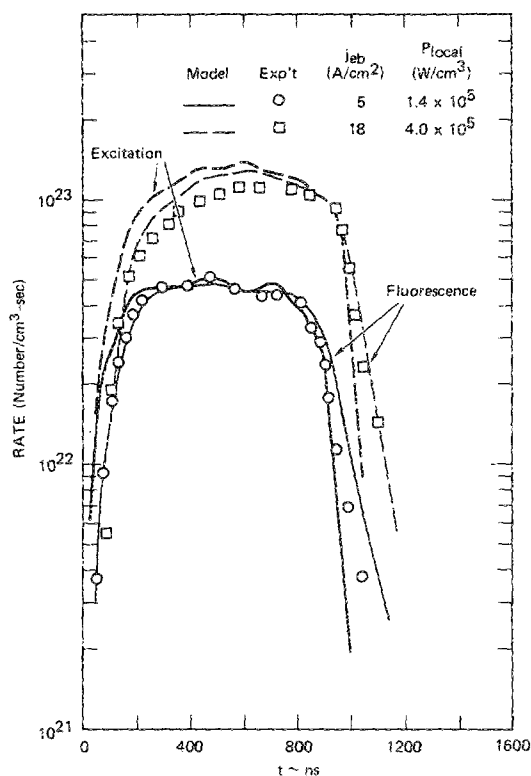
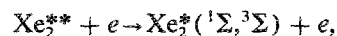
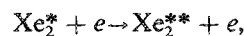


FIG. 5. Excitation rate and excimer fluorescence rate histories for *e*-beam-pumped xenon at 3 atm.

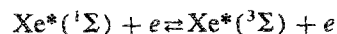
time and magnitude with increasing pressure and/or decreasing pump rate. In particular, the $\frac{1}{2}$ -atm data show fluorescence levels substantially below the pump levels during the pulse, with the fluorescence suppressed to a greater extent at higher pump levels. At this pressure, one is surprised to note that the fluorescence increases upon termination of the pump pulse, reaching its maximum value 150–200 ns later. At 1 atm, the correlation between pump rates and fluorescence rates is much clearer, although there is still a noticeable falloff of fluorescence efficiency with increasing pump rate. At 2 and 3 atm, the fluorescence followed the pump rate very closely.

The optimization of the kinetic model consisted primarily of an effort to achieve agreement between predictions of the model and experimental results like those presented in Figs. 3–5. The code predictions shown in those figures are the results of that optimization, and, in general, represent excellent agreement between model and experiment (all results are absolute; there is no normalization between experiment and model). It should be noted that good agreement between code predictions and experiments was achieved quite readily for the higher-pressure cases ($p \geq 2$ atm), where the code results were fairly insensitive to details of the kinetic model. Comparison with the lower pressure data, and particularly the $p = \frac{1}{2}$ atm data, provided a much more critical test for the model. When reaction rates were available from experiment, they were held fixed in the model. Other rates were varied to achieve the best fit to the data. The rates which caused the greatest variations in predicted fluorescence histories are noted in Table I.

Examination of the kinetics code calculations indicates that the electron interactions with both the atomic and molecular manifolds are important, even tending to dominate the neutral processes at the lower pressures. For example, we found that at 0.5 atm, electron mixing of Xe^* and Xe^{**} and of Xe_2^* and Xe_2^{**} is sufficiently fast to essentially keep these levels in equilibrium at the electron temperature. In fact, our deduced electron interaction rates indicate that electron mixing of the singlet and triplet excimers takes place primarily by cycling through the Xe_2^{**} level:



and that the direct mixing process



is only important in the afterglow where the electron temperature has dropped to a low value.

Furthermore, electron-induced dissociation of excimers (reactions 22 and 23 followed by reactions 6 or 7) is very important. At lower pressures, this process keeps the majority of the excited state population in the atomic manifold. At 0.5 atm, three-fourths of the excited population is in the Xe^* state. When the electron beam shuts off, the dissociation stops, and the suddenly uncountered three-body association causes a rapid increase in the Xe_2^* population (primarily the $^3\Sigma$ state), producing the increase in emission observed in the 0.5 atm intensity histories. This increase is seen to be more pronounced at the higher pump rate, as expected because of the higher electron density. At higher pressures, three-body association is increasingly faster than the electron-induced dissociation, and the population balance is driven toward the molecular manifold.

As is evident from Figs. 3–5 and the above discussion, there are significant loss mechanisms in the kinetic chain that reduce the fluorescence rate below the pump rate, particularly at low pressures and/or high pump rates. Our kinetic model indicates that the dominant quenching process at low pressures is superelastic collisions of electrons on Xe^* (reaction 21). At higher pressures, superelastic collisions on Xe_2^* (reaction 20) become dominant due to the shift in population balance from Xe^* to Xe_2^* , but then quenching rates are relatively small compared to the excimer radiative rates. Penning ionization losses (reactions 16–17 and 30–31) are smaller than the superelastic losses except in the afterglow.

It has been pointed out³⁹ that superelastic collisions of electrons on Xe^* cannot fully account for the low-pressure quenching since the energetic electron so produced will most likely reexcite a xenon atom in a subsequent collision (an effect which we have not included in our model). In considering other loss mechanisms, Huestis⁴⁰ pointed out that there are a very large number of xenon higher excited states lumped into a single level called Xe^{**} in current kinetic models. Since electron mixing tends to keep these excited states in equilibrium at the electron temperature, the populations calculated for Xe^{**} are large, but would be much larger if the true number of Xe^{**} states were included, for example, by setting the degeneracy factors $g^{**}/g^* \gg 1$ (currently, $g^{**}/g^* = 1$ in the model). Penning ionization losses would

increase in proportion to the square of the increased population of Xe^{**} , and could then become the dominant loss mechanism. Examination of the code results indicates that the population of Xe^{**} would have to increase by a factor of ~ 15 for this to be the case.

B. Fluorescence yields

The radiation efficiency of an e -beam-excited gas can be expressed in two ways. The first is to calculate the fluorescence energy efficiency, defined as

$$\eta_{\text{fluor}} = \frac{E_{\text{rad}}}{E_{\text{dep}}} = \frac{E_{\text{rad}}}{E_{\text{rad}} + E_{\text{heat}}},$$

where we have identified the fact that the radiating and heating components of energy deposition are expected to be of comparable value and both must be considered. The second expression of radiative efficiency is the fluorescence yield, defined as

$$\text{FY} = \frac{\int (\text{photon flux}/\text{cm}^3 \text{ s}) dt}{\int (\text{excited states produced}/\text{cm}^3 \text{ s}) dt}.$$

Such integrations can be done directly from the curves of Figs. 3–5, for example. The two expressions are related by the ratio of the average energy per excited state, E^* , to the Xe_2^* photon energy ($E_{\text{ph}} = 7.2 \text{ eV}$) simply as

$$\text{FY} = (E^*/E_{\text{ph}}) \eta_{\text{fluor}}.$$

The energy efficiency can be measured directly, while the fluorescence yield depends on the choice of E^* . Using our assumptions, $\text{FY} = 1$ and $\eta_{\text{fluor}} = 0.43$ represent ideal fluorescence performance.

The fluorescence yield for pure xenon and for xenon-argon mixtures measured in our program are summarized in Fig. 6. The results for pure xenon exemplify the behavior described above. That is, at $p = 1/2 \text{ atm}$, FY is always less than unity, and drops off rapidly with increasing pump rate. This effect is substantially reduced at $p = 1 \text{ atm}$, and by $p = 2\text{--}3 \text{ atm}$, the yields are near unity. The predictions of the kinetic code are also shown in Fig. 6; they are seen to be in good agreement with the experiments.

We also present in Fig. 6 an envelope of fluorescence efficiencies for xenon/argon mixtures with $3 \leq p_{\text{Ar}} \leq 10 \text{ atm}$ and $1/4 \leq p_{\text{Xe}} \leq 2 \text{ atm}$. These efficiencies are substantially

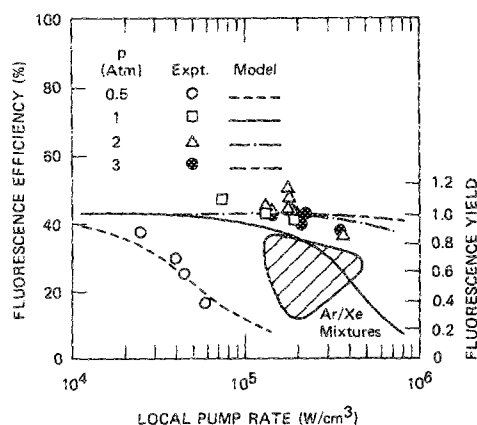


FIG. 6. Excimer fluorescence efficiencies for e -beam-pumped xenon.

lower than those for pure xenon at comparable pump rates. This result is in contrast to earlier observations⁴¹ of improved performance of the Xe_2^* laser when Ar/Xe mixtures were used in place of pure xenon. Johnson and Gerardo⁴² also observed a lower fluorescence efficiency in Xe/Ar mixtures than in pure xenon, although the change was not as great as observed here. In both of those studies, the pump rates and total pressures were substantially different from our conditions. We have not attempted to model the mixed gas tests.

C. Laser performance

When the gas cell was fitted with internal mirrors, lasing was fairly readily achieved at pressures of xenon of 2 atm and above. A typical laser time history is shown in Fig. 7, together with the corresponding sidelight fluorescence history. The laser turns on at about 500 ns and turns off when the pump pulse terminates. It was expected that a higher pump rate would cause earlier laser ring-up, with termination again coinciding with that of the pump, but in fact the laser terminated in the middle of the pump pulse after exhibiting laser action for about 200 ns, as illustrated in Fig. 8. This behavior was completely typical; in no case did lasing persist longer than about 200 ns. Similar observations have been reported in Refs. 13 and 14.

Based on the laser intensity measured by the calibrated photodiode and using the vendor-specified transmission of the laser output mirror, we calculated the internal cavity flux as indicated in Fig. 8. The laser beam cross section is not known, but we estimate it to be approximately $\frac{1}{4} \text{ cm}^2$. Then, the total cavity flux was on the order of 1 MW/cm^2 . For comparison, the saturation flux for the Xe_2^* transition is

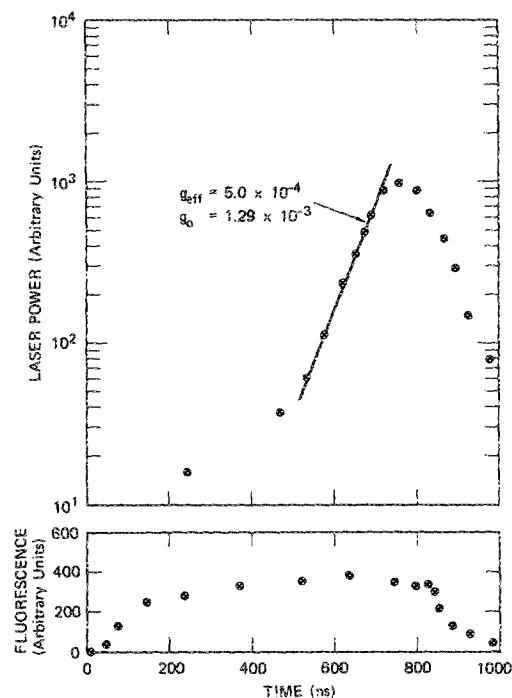


FIG. 7. Excimer laser and fluorescence histories for xenon at 2.5 atm pumped at 10 A/cm^2 ($P_{\text{local}} \approx 2 \times 10^5 \text{ W/cm}^2$).

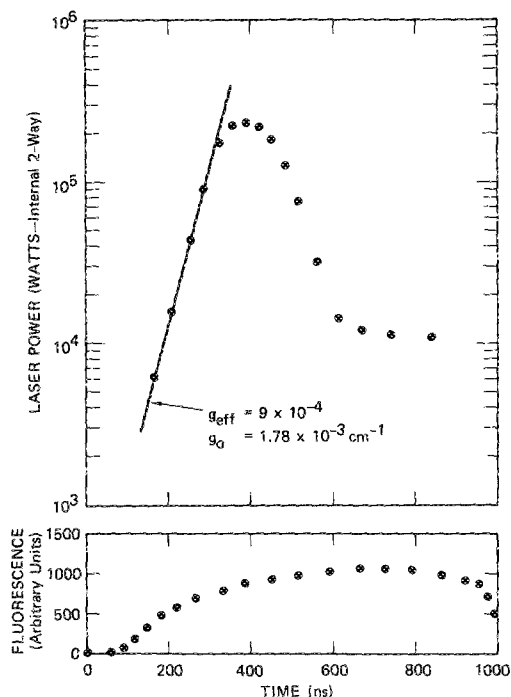


FIG. 8. Excimer laser and fluorescence histories for xenon at 3 atm pumped at 18 A/cm² ($P_{\text{local}} \approx 3 \times 10^5$ W/cm³).

~12 MW/cm². Thus, the laser extraction efficiency in our experiments was extremely low, consistent with measured laser energies of a few millijoules.

As noted above, lasing in pure xenon could only be achieved for $p_{\text{Xe}} \geq 2$ atm. The laser peak wavelength occurred at 172.7 nm, with $\Delta\lambda \approx 2$ nm. Lasing was also achieved in Ar/Xe mixtures, but it was still necessary to have a minimum of 2 atm of xenon, regardless of the argon pressure. When argon was present, the laser wavelength shifted to 172.2 nm with a bandwidth of ~2.4 nm.

As indicated in Figs. 7 and 8, the laser buildup was exponential over a large range of intensity. This allowed calculations of gain according to the simple formula $I/I_0 = \exp(gct)$. In the figures are listed both the effective gain and the intrinsic gain in the laser medium (g_0) after accounting for mirror losses and the ratio of active to total cavity lengths. The intrinsic gains calculated in this way are summarized in Fig. 9, plotted against the pump rate on the optical axis, P_{local} , which was determined as described above. The observed gains are seen to be proportional to the pump rate, roughly independent of gas composition. However, a comparison with the dashed line shows that the measured gains were only about 20% of the values that would be anticipated in the absence of absorption or photoionization losses.

The cross section for photoionization of Xe^{*} excimers was initially assumed to be $\sigma_{\text{pi}} = 2 \times 10^{-18}$ cm², as calculated by Huestis.²⁶ Modeling of the experimental laser intensity data using the kinetics and extraction code showed that the observed gains could be predicted very well if $\sigma_{\text{pi}} = 3.5 \times 10^{-18}$ cm². (This is within the factor-of-2 uncertainty quoted for Huestis' calculation.) Alternately, the gain

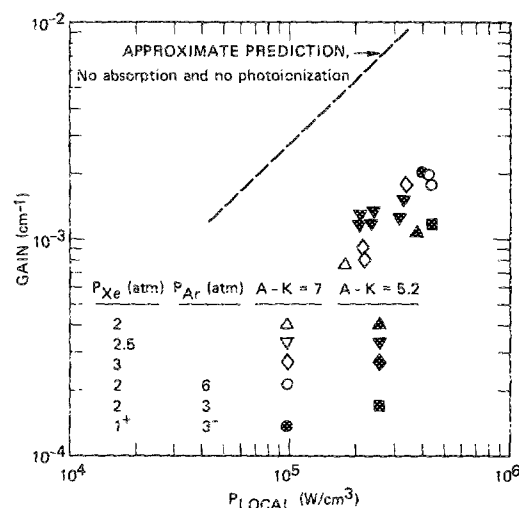


FIG. 9. Comparison of measured gains with values predicted if there were no absorption or photoionization losses.

can be predicted if $\sigma_{\text{pi}} = 2 \times 10^{-18}$ cm² and there is an additional absorption introduced of magnitude $\alpha = 1.1 \times 10^{-3}$ /cm. Such absorption could be due to impurities or to an excited atomic or molecular state of xenon. Regardless of the cause of the absorption, the small ratio of gain to absorption ($g_0/g_a \approx 0.25$) means that the achievable laser efficiency will be very small. It can be shown either from the code calculations or from solutions to simplified steady-state equations that the extraction efficiency will not exceed 1% under such a low ratio of gain to absorption.

The second important aspect of Xe^{*} laser performance is the early pulse termination as illustrated in Fig. 8. There are two possible explanations for this behavior. The first is that the absorption is time dependent in a different way than the gain, so that the net gain becomes zero or negative during the pulse. This would imply that the absorbing species is not Xe^{*}, nor does it have a constant population ratio to Xe^{*} (so that it would probably not be a state of Xe or Xe₂). The second possibility is that the laser mirrors change reflectivity during the laser pulse because of mirror coating absorption. It has long been known that Xe^{*} laser mirrors can be damaged or destroyed in a single shot when high pump rates are used,⁴³⁻⁴⁵ and, indeed, changing mirror reflectivity has been proposed previously as a pulse termination mechanism.^{13,42} Recently, it was shown that high-energy Xe^{*} laser pulse lengths could be extended if total internal reflectors were substituted for coated mirrors to form the laser cavity.⁴⁶

We cannot be sure that the high absorption levels observed in our laser tests do not change with time. But we have observed permanent visible damage to our dielectric-coated laser mirrors after a single laser pulse, which leads us to believe that changing mirror reflectivity contributes substantially to laser pulse termination. As noted earlier, our mirrors initially had about 96% reflectivity. Our net laser gain was sufficiently low (e.g., 1.78×10^{-3} /cm from Fig. 8) that a reduction in reflectivity to about 80% would terminate the laser pulse. ACTON Research measured the reflectivity

tivity of a damaged spot on one of our mirrors and found a value of 83%; however, it is not unreasonable to assume that the reflectivity might have been even lower during the pulse while the coating was at high temperature. In fact, the exponential decay constant for the laser intensity in Fig. 8 is consistent with a mirror reflectivity of $\sim 65\%$.

D. Electron density measurements

We made a quick survey of CO_2 laser transmission histories for the range of xenon pressures and pump rates of interest in this study with the intent of determining electron densities by inverse bremsstrahlung absorption. In all of these tests, the infrared detector signal increased during the pulse, as though the CO_2 laser was being amplified. In subsequent tests⁴⁷ we determined that the CO_2 laser intensity at the detector was being overwhelmed by superfluorescence on the $\text{Xe}(5d_4 \rightarrow 6p_3)$ atomic transition at $3.5 \mu\text{m}$. When a $10\text{-}\mu\text{m}$ filter was placed in front of the IR detector, a true absorption history was obtained as shown in Fig. 10. Also shown in the figure are absorption coefficients calculated for a similar run using the kinetic model. The agreement in absolute value is quite good, but the time dependencies are different. The experiment shows a linear increase in absorption during the main part of the pulse (200–900 ns), whereas the calculated absorption coefficient is nearly constant in the same time interval. The calculation results from approximately steady state values for the electron density ($n_e \approx 4 \times 10^{14}/\text{cm}^3$) and electron temperature ($T_e \sim 1 \text{ eV}$), which also gives a constant absorption coefficient ($\sigma = 2.2 \times 10^{-17} \text{ cm}^2$ at 2 atm of Xe). The reasons for the discrepancy are not apparent, although it should be noted that an increase of the electron temperature from 1 to 1.3 eV during the pulse would change the absorption coefficient to match the experiments.

V. CONCLUSIONS

These experiments have shown that the performance of Xe_2^* as a VUV source in the fluorescence mode is excellent. Fluorescence yields of unity and fluorescence energy efficiencies at the theoretical maximum near 50% are readily achieved at modest pressures (2–3 atm) for local pump rates around 10^5 W/cm^2 , and maximum efficiencies should exist for pump rates above 10^6 W/cm^2 at slightly higher pres-

ures. The laser performance of Xe_2^* at 172 nm, however, is quite poor. The intrinsic extraction efficiency under these pump conditions is limited to $< 1\%$ by a high absorption in the laser medium that is probably due to photoionization of the Xe_2^* ($^3\Sigma_u^+, ^1\Sigma_u^+$) excimers. Poor laser performance is further exacerbated by a pulse termination mechanism that prevents achievement of saturation intensities in the laser cavity. There is considerable evidence that this termination is due to reduced mirror reflectivities induced by absorption in the mirror coatings.

The kinetics model for e -beam-pumped xenon has been substantially improved through the addition of several reactions accounting for the interaction between secondary electrons and excited xenon atomic and molecular states. These reactions are the dominant kinetic processes at the lower pressures investigated. With this improved model, we have been able to achieve good agreement between absolute calculated and experimental fluorescence histories for pressures as low as 0.5 atm. Nevertheless, there are still some uncertainties to be resolved. For example, there is some question about the mechanism of quenching of fluorescence at high pump rates and/or low pressures. There is not complete agreement between the electron density and electron temperature histories as deduced from inverse bremsstrahlung absorption measurements and from the predictions of the kinetic model. Finally, the excited state(s) responsible for the strong absorption at 172 nm have not been positively identified. It should also be noted that there is no mechanism in the kinetic model which would account for strong population inversions in the atomic xenon excited state manifold as manifested by superradiant emission on the $3.51\text{-}\mu\text{m}$ transition.

ACKNOWLEDGMENTS

The contributions of Dr. Charles K. Rhodes to the development of excimer lasers and photolytically pumped energy storage lasers, and to the establishment and guidance of this research are gratefully acknowledged. The technical interest and support of Dr. Paul W. Hoff are also greatly appreciated. This work was supported by the Department of Energy, Division of Laser Fusion, under Contract No. DE-AC05-78DPO5606.

APPENDIX: RATES FOR INTERACTIONS OF ELECTRONS WITH EXCITED XENON

The kinetics of e -beam-pumped xenon are strongly dependent upon the interactions of the secondary electrons with the excited Xe and Xe_2 states. Because of the importance of these rates to the modeling effort and the general lack of cross sections for electron-excited state interactions, it was necessary to estimate these cross sections using various applicable theoretical techniques. We consider three classes of reaction: (1) ionization of excited states, (b) excitations between two states with an optically allowed transition, and (c) excitations when the transition is optically forbidden.

We have calculated the required excited state ionization cross sections by the classical binary encounter method us-

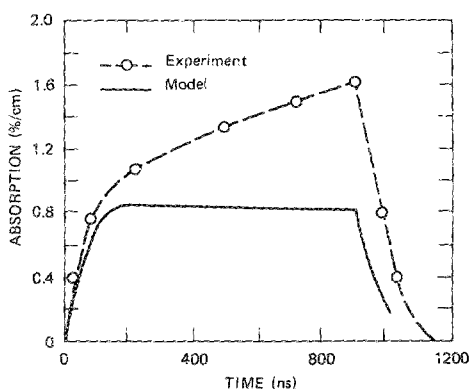


FIG. 10. Inverse bremsstrahlung absorption at $10.6 \mu\text{m}$ in xenon at 2 atm pumped at 10 A/cm^2 ($P_{\text{total}} \approx 1.5 \times 10^5 \text{ W/cm}^2$).

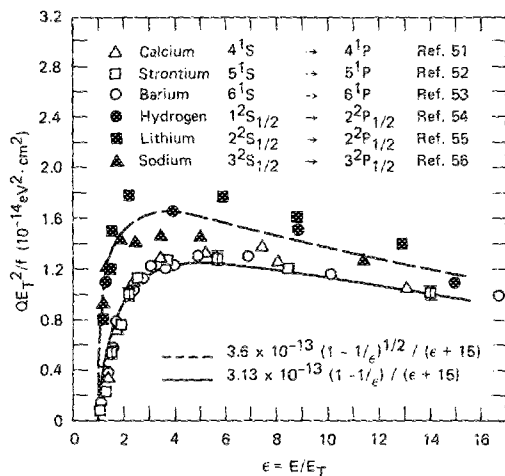


FIG. 11. Absolute cross sections for electron excitation of optically allowed transitions.

ing the formulas developed by Vriens.⁴⁸ These cross sections appear to be reliable to $\pm 50\%$.

For optically allowed transitions, the cross sections for excitation between two states can be obtained from a simple scaling rule that is based on the Born approximation. As the Born approximation suggests,^{49,50} the cross section in the high-energy limit can be written

$$\sigma(\epsilon) = K(f/E_T^2)g(\epsilon), \quad (A1)$$

where E_T is the transition energy, f is the optical oscillator strength, $\epsilon = E/E_T$, E is the electron energy, and K is a constant. It is found experimentally that $g(\epsilon)$ is a nearly universal function that is somewhat dependent on the structure of the atom and the transition involved but which describes the cross section energy dependence all the way to threshold. The function $g(\epsilon)$ can be obtained from experimental measurements of allowed transitions that have been carried out on the ground states of alkali and alkaline earth atoms. Plots of recent absolute cross section measurements⁵¹⁻⁵⁶ are presented in Fig. 11, together with simple functional forms of $g(\epsilon)$ that provide very accurate fits to the data from threshold to high energies. It is useful to note that $g(\epsilon)$ is a universal function for all energies for a specific type of atom. Clearly, the threshold dependence is somewhat steeper for the $ns-np$ transition in the single electron case (IA) than it is for the two electron (IIA). The alkali case is well represented by

$$Kg(\epsilon) = \frac{3.6 \times 10^{-13}}{\epsilon + 15} (1 - 1/\epsilon)^{1/2} \text{ eV}^2 \text{ cm}^2, \quad (A2)$$

and the alkaline earth cross sections are represented by

$$Kg(\epsilon) = \frac{3.1 \times 10^{-13}}{\epsilon + 15} (1 - 1/\epsilon) \text{ eV}^2 \text{ cm}^2. \quad (A3)$$

These simple functions fit the data very well and are useful for determining rate constants. The reduced cross-section function (A3) was used, together with appropriate f numbers, to determine several of the electron rates between excited states of Xe and Xe₂. The deexcitation (superelastic) cross sections were obtained from the inelastic cross sections by the detailed balance relationship

$$\sigma_{21}(E) = \left(\frac{2J_1 + 1}{2J_2 + 1} \right) \left(\frac{E + E_T}{E} \right) \sigma_{12}(E + E_T), \quad (A4)$$

where the J 's represent the multiplicities of the upper and lower states.

For forbidden optical transitions where electron exchange is the major mechanism by which a transition is induced, a reliable method of estimating cross sections does not exist. In a few cases, cross sections have been measured for excitation of metastable levels from the ground state (e.g., helium and other rare gases). Beyond these results, the only excited state-excited state cross sections available are some theoretical results for hydrogen and helium.^{57,58} Typically, exchange cross sections for forbidden transitions rise steeply from threshold to a peak and then fall off more rapidly with increasing energy than do those for allowed transitions. Using the calculated cross sections in helium as a guide, we have determined that an energy-dependent function of the form

$$\sigma_{12} = (\sigma_0/\epsilon^2) [1 - (1/\epsilon)] \quad (A5)$$

fits many of the excited state cross sections. However, no generalized rule for scaling the magnitude of the cross sections to different transitions or different elements has been discovered. Our initial cross sections for Xe₂(³Σ) - Xe₂(¹Σ) mixing (Table I, reaction 10) were obtained by scaling from similar transitions in helium according to $(E_T)^{-2}$. This scaling certainly is not justified for all transitions. Much more experimental and theoretical effort

TABLE II. Estimated cross sections for electron interactions with excited states of xenon.

Reaction (See Table I)	Cross sections (cm ²)	Energy range
10a	$Q(E) = \frac{1.8 \times 10^{-15}}{E^2} \left(1 - \frac{0.063}{E} \right)^{1/2}$	$E \geq 0.063 \text{ eV}$
10b	$Q(E) = \frac{5.4 \times 10^{-15}}{E^{1/2} (E + 0.063)^{3/2}}$	$E > 0$
18	$Q(E) = \frac{6.5 \times 10^{-14}}{E + 10.8} \left(0.5 - \frac{1}{E} - \frac{2.2}{E^2} \right)$	$E \geq 3.3$
19	$Q(E) = \frac{6.5 \times 10^{-14}}{E + 12.2} \left(0.45 - \frac{1}{E} - \frac{2.5}{E^2} \right)$	$E \geq 3.8$
20	$Q(E) = \frac{9.7 \times 10^{-15}}{E + 115}$	$E \geq 0$
21	$Q(E) = \frac{8.3 \times 10^{-15}}{E + 133}$	$E \geq 0$
22	$Q(E) = \frac{4.6 \times 10^{-13}}{E + 22.5} \left(1 - \frac{1.5}{E} \right)$	$E > 1.5$
23,27	$Q(E) = \frac{3.1 \times 10^{-13}}{E + 15} \left(1 - \frac{1}{E} \right)$	$E > 1$
24a	$Q(E) = \frac{2.3 \times 10^{-13}}{E + 16}$	$E \geq 0$
24b	$Q(E) = \frac{7.8 \times 10^{-14}}{E + 16}$	$E \geq 0$
28	$Q(E) = \frac{3.1 \times 10^{-13}}{E + 16}$	$E \geq 0$
26	$Q(E) = \frac{6.5 \times 10^{-14}}{E + 8} \left(0.67 - \frac{1}{E} - \frac{1.7}{E^2} \right)$	$E \geq 2.5$
32	$Q(E) = \frac{2.3 \times 10^{-13}}{E + 22.5} \left(1 - \frac{1.5}{E} \right)$	$E \geq 1.5$
33	$Q(E) = \frac{6.5 \times 10^{-14}}{E + 8} \left(0.72 - \frac{1}{E} - \frac{1.5}{E^2} \right)$	$E \geq 2.3$

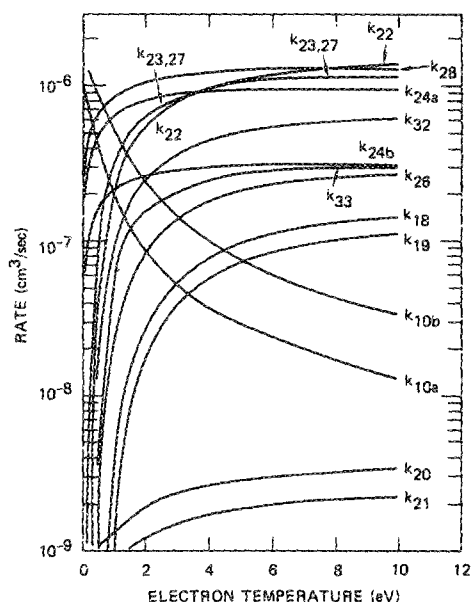


FIG. 12. Estimated rate coefficients for electron interactions with excited states of xenon assuming a Maxwellian electron energy distribution. For identification of reactions, see Table I.

should be devoted to finding appropriate scaling rules for cross sections of forbidden transitions.

Using the above techniques, we have estimated energy-dependent cross sections for all the electron-excited state reactions of Table I. The results are given in Table II, together with the valid range of electron energy. These cross sections have been convolved with a Maxwellian electron energy distribution to determine the kinetic rates as a function of electron temperature T_e shown in Fig. 12. These rates were used as the starting point for calculations with the kinetic code in Sec. II. The rates were varied to examine the effects on the fit of the code predictions to the data. It was found that the estimated rates provided optimum results without adjustment with two exceptions. First, the superelastic quenching rates k_{20} and k_{21} were increased by a factor of 3 to provide the required magnitude of losses as discussed in Sec. IV. Second, the singlet-triplet excimer mixing rate k_{10} was reduced by an order of magnitude in order to fit experimental fluorescence decay curves. This rate is for an optically forbidden transition, and thus has the scaling uncertainty described above, so that an adjustment is not surprising. It should be noted that there is an experimental measurement of this rate⁶⁰ which gave the value $k_{10a} = 2 \times 10^{-6} \text{ cm}^3/\text{s}$. The electron temperature was not specified in those measurements, but it was probably near room temperature since the elastic cooling time for electrons in xenon at the 10 atm measurement pressure is on the order of 10 ns, while the observed decay times were near 100 ns. Our estimate for low T_e is $\sim 10^{-6} \text{ cm}^3/\text{s}$, which is in good agreement with the previous experiment but in disagreement with the magnitude required for the code to fit the present data.

¹J. R. Murray and C. K. Rhodes, *J. Appl. Phys.* **45**, 5041 (1976).

²W. M. Hughes, N. T. Olson, and R. Hunter, *Appl. Phys. Lett.* **28**, 81 (1976).

- ³N. G. Basov, Yu. A. Babeiko, V. S. Zuev, L. D. Mikheev, V. K. Orlov, I. V. Pogorelskii, D. B. Stavroskii, A. V. Startsev, and V. I. Yalovoi, *Sov. J. Quantum Electron.* **6**, 505 (1976).
- ⁴I. S. Datskevich, V. S. Zuev, L. D. Mikheev, and I. V. Pogorelskii, *Sov. J. Quantum Electron.* **8**, 831 (1978).
- ⁵H. T. Powell and J. J. Ewing, *Appl. Phys. Lett.* **33**, 165 (1978).
- ⁶H. T. Powell, D. Prosnitz, and B. R. Schleicher, *Appl. Phys. Lett.* **34**, 571 (1979).
- ⁷J. G. Eden, *Appl. Phys. Lett.* **33**, 495 (1978).
- ⁸J. G. Eden, *Opt. Lett.* **3**, 94 (1978).
- ⁹W. K. Bischel, H. H. Nakano, D. J. Eckstrom, R. M. Hill, D. L. Huestis, and D. C. Lorents, *Appl. Phys. Lett.* **34**, 565 (1979); D. J. Eckstrom and H. C. Walker, Jr., *IEEE J. Quantum Electron.* **QE-18**, 176 (1982).
- ¹⁰H. T. Powell and R. E. Wilder, Topical Meeting on Excimer Lasers, Charleston, South Carolina, September, 1979 (unpublished).
- ¹¹N. G. Basov, V. A. Danilychev, and Yu. M. Popov, *Sov. J. Quantum Electron.* **1**, 18 (1971).
- ¹²C. E. Turner, Jr., *Appl. Phys. Lett.* **31**, 659 (1977).
- ¹³J. D. Campbell and R. E. Center, *J. Appl. Phys.* **51**, 2348 (1980).
- ¹⁴C. Duzy and M. J. W. Boness, *Appl. Phys. Lett.* **35**, 903 (1979); C. Duzy and J. Boness, *IEEE J. Quantum Electron.* **QE-16**, 640 (1980).
- ¹⁵D. C. Lorents and R. E. Olson, Semiannual Technical Report No. 1, Contract No. N00014-72-C-0457, Stanford Research Institute, December, 1972; D. C. Lorents, *Physica* **82C**, 19 (1976).
- ¹⁶C. W. Werner, E. V. George, P. W. Hoff, and C. K. Rhodes, *Appl. Phys. Lett.* **25**, 235 (1974).
- ¹⁷C. W. Werner, E. V. George, P. W. Hoff, and C. K. Rhodes, *IEEE J. Quantum Electron.* **QE-13**, 769 (1977).
- ¹⁸L. R. Peterson and J. E. Allen, *J. Chem. Phys.* **56**, 6068 (1972).
- ¹⁹A. P. Vitois and H. J. Oskam, *Phys. Rev. A* **8**, 1860 (1973).
- ²⁰A. K. Bhattacharya, *Appl. Phys. Lett.* **17**, 521 (1970).
- ²¹C. W. Werner, E. Zamir, and E. V. George, *Appl. Phys. Lett.* **29**, 236 (1976).
- ²²Y.-J. Shiu, M. A. Biondi, and D. P. Sipler, *Phys. Rev. A* **15**, 494 (1977).
- ²³P. R. Timpson and J. M. Anderson, *Can. J. Phys.* **48**, 1817 (1970).
- ²⁴J. H. Kolts and D. W. Setser, *J. Chem. Phys.* **68**, 4848 (1978).
- ²⁵T. D. Bonifield, F. H. K. Rambow, G. K. Walters, M. J. McCusker, D. C. Lorents, and R. A. Gutcheck, *J. Chem. Phys.* **72**, 2914 (1980).
- ²⁶D. L. Huestis, in D. C. Lorents, D. J. Eckstrom, and D. L. Huestis, Report No. MP 73-2, Stanford Research Institute, Menlo Park, CA (September, 1973) (unpublished).
- ²⁷T. N. Rescigno, A. U. Hazi, and A. E. Orel, *J. Chem. Phys.* **68**, 5283 (1978).
- ²⁸E. Zamir, C. W. Werner, W. P. Lapatovich, and E. V. George, *Appl. Phys. Lett.* **27**, 56 (1975).
- ²⁹W. L. Morgan (private communication).
- ³⁰C. J. Elliott and A. E. Greene, *J. Appl. Phys.* **47**, 2946 (1976).
- ³¹H. S. Heaps and G. Herzberg, *Z. Phys.* **133**, 48 (1952).
- ³²F. Mies, *Mol. Phys.* **26**, 1233 (1973).
- ³³P. M. Stefan (private communication).
- ³⁴H. M. Colbert, "A Computer Program for Calculating Combined Photon-Electron Transport in Complex Systems," Report No. SLL-74-0012, Sandia Livermore Laboratories, 1974.
- ³⁵D. J. Eckstrom and H. C. Walker, Jr., *J. Appl. Phys.* **51**, 2458 (1980).
- ³⁶G. Bekefi, *Radiation Processes in Plasmas* (Wiley, New York, 1966).
- ³⁷J. B. Gerardo and A. W. Johnson, *IEEE J. Quantum Electron.* **QE-9**, 748 (1973).
- ³⁸A. W. Johnson and J. B. Gerardo, *J. Appl. Phys.* **46**, 4870 (1975).
- ³⁹P. W. Hoff (private communication).
- ⁴⁰D. L. Huestis (private communication).
- ⁴¹P. W. Hoff, J. C. Swingle, and C. K. Rhodes, *Appl. Phys. Lett.* **5**, 245 (1973).
- ⁴²A. W. Johnson and J. B. Gerardo, *J. Appl. Phys.* **45**, 867 (1974).
- ⁴³E. R. Ault, M. L. Bhaumik, W. M. Hughes, R. J. Jensen, C. P. Robinson, A. C. Kolb, and J. Shannon, *IEEE J. Quantum Electron.* **QE-9**, 1031 (1973).
- ⁴⁴P. W. Hoff, J. C. Swingle, and C. K. Rhodes, *Opt. Commun.* **8**, 128 (1973).
- ⁴⁵W. M. Hughes, J. Shannon, and R. Hunter, *Appl. Phys. Lett.* **25**, 85 (1974).
- ⁴⁶P. D. Slade and G. R. Fournier, *Opt. Commun.* **29**, 325 (1979).
- ⁴⁷T. Rothem, H. C. Walker, Jr., and D. J. Eckstrom (unpublished).
- ⁴⁸L. Vriens, *Case Studies in Atomic Collision Physics I*, edited by E. W. McDaniel and M. R. C. McDowell (North-Holland, Amsterdam, 1969), Chap. 6.

- ⁴⁹A. E. S. Green, *AIAA J.* **4**, 769 (1966).
- ⁵⁰M. Inokuti, *Rev. Mod. Phys.* **43**, 297 (1971).
- ⁵¹V. J. Ehlers and A. Gallagher, *Phys. Rev. A* **7**, 1573 (1976).
- ⁵²S. T. Chen, D. Leep, and A. Gallagher, *Phys. Rev. A* **13**, 947 (1976).
- ⁵³D. Leep and A. Gallagher, *Phys. A* **10**, 1082 (1976).
- ⁵⁴R. Long, D. Cox, and S. Smith, *J. Res. Natl. Bur. Stand. A* **72**, 521 (1968).
- ⁵⁵S. T. Chen and A. Gallagher, *Phys. Rev. A* **14**, 593 (1974).
- ⁵⁶E. A. Enmark and A. Gallagher, *Phys. Rev. A* **6**, 192 (1972).
- ⁵⁷P. G. Burke, J. W. Cooper, and S. Ormonde, *Phys. Rev.* **183**, 245 (1969).
- ⁵⁸M. R. Flannery and K. J. McCann, *Phys. Rev. A* **12**, 846 (1975).
- ⁵⁹G. A. Khayrallah, S. T. Chen, and J. R. Rumble, Jr., *Phys. Rev. A* **17**, 513 (1978).
- ⁶⁰J. W. Keto, R. E. Gleason, Jr., T. D. Bonifield, and G. K. Walters, *Chem. Phys. Lett.* **42**, 125 (1976).